

# Ferroelectric state in an $\alpha$ -Nd<sub>2</sub>WO<sub>6</sub> polymorph stabilized in a thin film

Thomas Carlier <sup>a,b</sup>, Marie-Hélène Chambrier <sup>a\*</sup>, Antonio Da Costa <sup>a</sup>, Florent Blanchard <sup>a</sup>, Thibaud Denneulin <sup>c,d</sup>, Manon Létiche <sup>a</sup>, Pascal Roussel <sup>a</sup>, Rachel Desfeux <sup>a</sup>, Anthony Ferri <sup>a</sup>

<sup>a</sup> Univ. Artois, CNRS, Centrale Lille, Univ. Lille, UMR 8181 – UCCS – Unité de Catalyse et Chimie du Solide, F-62300 Lens, France

<sup>b</sup> HORIBA FRANCE S.A.S., Boulevard Thomas Gobert, Passage Jobin Yvon, 91120 Palaiseau, France

<sup>c</sup> Ernst Ruska-Centre for Microscopy and Spectroscopy with Electrons and Peter Grünberg Institute, Forschungszentrum Jülich, 52425 Jülich, Germany

<sup>d</sup> CEMES, CNRS, 29 rue Jeanne Marvig, 31055 Toulouse, France

**KEYWORDS :** Nd<sub>2</sub>WO<sub>6</sub>, Thin Film, Pulsed Laser Deposition, High-Resolution X-Ray Diffraction, Transmission Electron Microscopy, Ferroelectricity, Piezoresponse Force Microscopy, Conductive Atomic Force Microscopy, Leakage Current, Strain Engineering.

---

**ABSTRACT:** Taking full advantage of strain engineering, (001)-epitaxial Nd<sub>2</sub>WO<sub>6</sub> (NdWO) thin films have been successfully grown on (001)-oriented SrTiO<sub>3</sub> single-crystal substrates by pulsed laser deposition. High-resolution X-ray diffraction characterizations highlight the stabilization of a new orthorhombic (*Pm2<sub>1</sub>n*) NdWO polymorphic form, isostructural to  $\alpha$ -La<sub>2</sub>WO<sub>6</sub>. Reciprocal Space Mappings (RSM) have been used in the determination of the NdWO thin film structure. Coupled to the  $2\theta$ - $\omega$  X-ray patterns, the cell parameters were calculated:  $a = 16.40(5)$  Å,  $b = 5.46(5)$  Å,  $c = 8.68(1)$  Å. X-ray-diffraction pole-figure measurements evidence the crystallographic relationships between the film and substrate:  $[100]_{\text{NdWO}} \parallel [110]_{\text{STO}}$ ,  $[010]_{\text{NdWO}} \parallel [1\bar{1}0]_{\text{STO}}$  and  $[001]_{\text{NdWO}} \parallel [001]_{\text{STO}}$ . In addition, robust piezoelectricity and ferroelectricity are revealed at room temperature through both local hysteresis loops and domain manipulation experiments using piezoresponse force microscopy technique. Typical polarization retention behaviour associated to specific nanoscale conduction are in good agreement with classical ferroelectric phenomenon in oxide materials. The successful observation of piezo-/ferroelectricity at room temperature in innovative strain-stabilized  $\alpha$ -NdWO thin films paves the way for new lead-free functional materials devoted for numerous applications, including actuators, sensors, or non-volatile memory devices.

---

## INTRODUCTION

Since World War II, advanced electronic devices based on piezoelectric and ferroelectric materials attracted a lot of attention and represent an important part of industrial-business and innovations, taking in mind the fact that piezo-/ferroelectric applications areas are wide ranging from consumer devices to high technology industries: laptops, sonars, frequency filters, gas sensors, data storage systems (Ferroelectric Random Access Memories (FeRAMs)), etc. Moreover, promising and impending technological developments such as energy harvesting, geothermal power plant sensors, aerospace, miniaturization still keep piezo-/ferroelectric materials highly attractive. Since the 40's, lead zirconate-titanate Pb(Zr,Ti)O<sub>3</sub> (PZT), <sup>[1,2]</sup>, (Pb,Li)(Zr,Ti)O<sub>3</sub> (PLZT) <sup>[3]</sup> or  $x\text{Pb}(\text{MgNb})\text{O}_3$ -(1- $x$ )PbTiO<sub>3</sub> (PMN-PT) <sup>[4]</sup> to cite the main ones of the well-known lead-based perovskite type family, have been in the first place on the market of such electromechanical materials. Indeed, PZT and derivatives show an exceptional piezo-/ferroelectric behavior: a relatively high Curie temperature around 500°C combined

with excellent piezoelectric properties. <sup>[5, 6, 7]</sup> It is interesting to note that since the 70's, plenty of patents for Pb-containing relaxor based on multi-layer piezo-/ferroelectric ceramic capacitor devices have been filed. All these strong patents encouraged companies such as Panasonic, Toshiba, NEC to develop substituted compounds and in this way to improve ferroelectric performances. <sup>[8]</sup>

However, in reference to the European Union legislations, REACH (*Registration, Evaluation, Authorization and Restriction of Chemicals*) classification, connected to the environmental concerns, has decreed that even if lead-based substances are still allowed for the moment, they have to be progressively replaced by less toxic substances. <sup>[9, 10]</sup>

In this context, new investigations have been conducted, mainly based on two strategies: either optimize well-known piezoelectric materials such as BaTiO<sub>3</sub> (BTO) <sup>[11]</sup> and K<sub>x</sub>Na<sub>1-x</sub>NbO<sub>3</sub> (KNN) <sup>[12]</sup>, or explore new systems. Our approach belongs to this last option.

Microstructure engineering (grain and domain size, texture) is a very powerful tool to enhance functional properties. For instance, for a ferroelectric compound, the best piezoelectric coefficient  $d_{33}$  is achieved for a single crystal while the worst  $d_{33}$  is observed for a random polycrystalline sample. <sup>[13]</sup> Thus, preferential orientation will play on the ferroelectric response. In other way, the grain size is also able to increase the piezoelectric coefficient by introducing grain constrains. <sup>[13]</sup> Moreover, since single crystal growth is generally difficult to produce at large scale, only polycrystalline or thin films are viable for mass production. In this context, thin film growth is very interesting because it provides an achievable intermediate between powder and single crystal. Consequently, thin films technology appears as an interesting way to obtain materials with enhanced piezo-/ferroelectric properties. Thin films such as  $\text{SrMnO}_3$ , <sup>[14]</sup>  $\text{SrTiO}_3$ , <sup>[15,16]</sup>  $\text{EuTiO}_3$ , <sup>[17]</sup>  $\text{BiFeO}_3$  <sup>[18]</sup> etc.... are already commonly obtained and their physical properties can be tuned using the substrate-strain induced.

The second strategy, that we privileged, is to explore the phase diagram in order to obtain new candidates showing functional properties. In this respect, two ways can be developed. The first one is playing with dopants and modifiers (isovalents, aliovalents dopants) in already known ferroelectric compounds, which involves the construction of new phase diagrams, such as for example the systems  $\text{Ba}_{(1-x)}\text{Ca}_x\text{Ti}_{(1-y)}\text{Zr}_y\text{O}_3$  (BCTZ), <sup>[19]</sup> KNN,  $(1-x)\text{Bi}_{1/2}\text{Na}_{1/2}\text{TiO}_3$ - $x\text{BaTiO}_3$  (BNT-BT). <sup>[20,21]</sup> The second way is to work on new systems in order to discover new piezo-/ferroelectric compounds. In the present work, this latter approach was used for lanthanide tungstate  $\text{Ln}_2\text{WO}_6$  systems because: i) some polymorphs are noncentrosymmetric and therefore susceptible to present ferroelectricity, ii) some tungsten bronze  $\text{K}_x\text{W}_2\text{O}_6$  are already known to form a ferroelectric class and also iii) dozen of papers deals with  $\text{Bi}_2\text{WO}_6$  compound and its ferroelectric and photocatalyst properties. <sup>[22]</sup> Indeed, the Curie temperature of  $\text{Bi}_2\text{WO}_6$  is very interesting because quite high ( $T_c = 940^\circ\text{C}$ ) which allows its use in gas injector or gas sensor at high temperature. <sup>[23]</sup>

Even if studies  $\text{A}_2\text{O}_3$ - $\text{MO}_3$  ( $\text{A} = \text{Ln}^{3+}$ ,  $\text{Bi}^{3+}$ ,  $\text{Y}^{3+}$ ,  $\text{Fe}^{3+}$ ,  $\text{Sc}^{3+}$  and  $\text{M} = \text{W}^{6+}$ ,  $\text{Mo}^{6+}$ ) phase diagram were intensive in 70's in order to determine their structure, nowadays some of these phase diagrams still remain incomplete in terms of characterization properties. Many application fields have already been determined for some of the definite compounds in this system such as ionic and mixed conduction, <sup>[24, 25]</sup> photocatalytic activities, <sup>[26]</sup> luminescence, <sup>[27]</sup> negative thermal expansion. <sup>[28]</sup> Concerning piezo-/ferroelectric properties, several works and even patents have been written for  $\text{A}_2\text{M}_3\text{O}_{12}$  ( $\text{A} = \text{Gd}$ ,  $\text{Tb}$  and  $\text{Eu}$ ,  $\text{Y}$ ;  $\text{M} = \text{W}$  and  $\text{Mo}$ ). <sup>[29, 30]</sup>

Moreover,  $\text{Ln}_2\text{O}_3$ - $\text{WO}_3$  systems are interesting because of the low cost of both lanthanide and tungsten elements and also because of the low toxicity of these elements, which anticipates both European decrees and also industrial constraints. In terms of piezoelectric properties, lanthanide elements are interesting because of their high

polarizability with for instance values of  $6.07 \text{ \AA}^3$  and  $5.01 \text{ \AA}^3$  for lanthanum and neodymium, respectively, (maximum is observed for Cs:  $7.43 \text{ \AA}^3$  whereas minimum is observed for Al  $0.79 \text{ \AA}^3$ ), which place first lanthanide elements in the top of the polarizability scale.

Concerning  $\text{Ln}_2\text{WO}_6$  compounds, they are known in the literature since 1902 thanks to Cleve's study on  $\text{Yb}_2\text{WO}_6$ . Later, in 1973, Brixner *et al.* reported refined cell parameters of the  $\text{Ln}_2\text{WO}_6$  ( $\text{Ln} = \text{Lanthanides except Ce}$ ). <sup>[31]</sup> They typically present structural arrangements based on the fluorite ( $\text{CaF}_2$ ) or Scheelite ( $\text{CaWO}_4$ ) structure type. A rich literature exists on this series, not only because of the several polymorphic phases but also because the different crystal structure stabilizations are dependent on the exact method of synthetic preparation. <sup>[32, 33, 34, 35, 36]</sup>

Depending on the lanthanide radius, three different tungstate structures are observed. <sup>[37,38]</sup>  $\text{La}_2\text{WO}_6$  presents two polymorphic structures depending on the temperature: i) the low temperature form,  $\beta\text{-La}_2\text{WO}_6$ , crystallizes in the space group  $P_{2,2,2_1}$  ( $n^\circ 19$ ) with cell parameters  $a = 7.5196(1) \text{ \AA}$ ,  $b = 10.3476(1) \text{ \AA}$ ,  $c = 12.7944(2) \text{ \AA}$ , <sup>[39]</sup> ii) the high temperature form, <sup>[40]</sup>  $\alpha\text{-La}_2\text{WO}_6$ , crystallizes in the space group  $Pm_{2,n}$  ( $n^\circ 31$ ) with cell parameters  $a = 16.5531(1) \text{ \AA}$ ,  $b = 5.52003(3) \text{ \AA}$ ,  $c = 8.88326(3) \text{ \AA}$ . A first order phase transition between beta and alpha occurs at  $1440^\circ\text{C}$ . The structure for the  $\alpha\text{-La}_2\text{WO}_6$  phase is closely related to the Scheelite one.

Recently, piezoelectricity and ferroelectricity within  $\alpha\text{-La}_2\text{WO}_6$  thin were locally evidenced by our group when stabilized on  $\text{SrTiO}_3$  or  $\text{LaAlO}_3$ . <sup>[41, 42]</sup>

On the one hand,  $\text{Ln}_2\text{WO}_6$  compounds with large cations ( $\text{Ln} = \text{Ce}$  to  $\text{Dy}$ ) usually crystallize in a monoclinic fluorine type-superstructure ( $C_c^2$ ;  $a_m \approx 3a_f$ ;  $b_m \approx 2b_f$ ;  $c_m \approx c_f$  and  $\beta \approx 107.7^\circ$ ). <sup>[43]</sup> On the other hand, for the smallest cations ( $\text{Ln} = \text{Ho}$  to  $\text{Lu}$ ) it results in a  $P_c^2$  space group. <sup>[44]</sup> Scheelite-type superstructure with following relationships:  $\vec{a}_m \approx \vec{b}_{sch} - \vec{a}_{sch}$ ;  $\vec{b}_m = \frac{\vec{c}_{sch}}{2}$ ;  $\vec{c}_m \approx 2\vec{a}_{sch} + \vec{b}_{sch}$ ;  $\beta_m \approx 108^\circ$ . <sup>[45]</sup>

At high temperature, all the  $\text{Ln}_2\text{WO}_6$  compounds with  $\text{Ln} = \text{Ce}$  to  $\text{Lu}$  undergo a phase transition ( $>1500^\circ\text{C}$ ) to a tetragonal compound.

Concerning  $\text{Nd}_2\text{WO}_6$ , Yoshimura *et al.* have reported in addition to a phase transition close to  $1430^\circ\text{C}$  between temperature prototypes, low and high another metastable phases. <sup>[46]</sup> The low temperature form crystallizes in the space group  $C_c^2$  ( $n^\circ 15$ ) with cell parameters  $a = 5.55(1) \text{ \AA}$ ,  $b = 11.38(1) \text{ \AA}$ ,  $c = 15.86(1) \text{ \AA}$ ,  $\beta = 107.7^\circ$ . The structure consists of two strongly distorted polyhedral: i) tungsten atoms are surrounded by five oxygen atoms, which build up an isolated trigonal bipyramid  $[\text{WO}_5]^{4-}$ ; ii) neodymium atoms are forming  $[\text{LnO}_8]^{10-}$  units (figure 1a).

The "intermediate temperature" form quoted from V by Efremov observed between  $1430^\circ\text{C}$  and  $1450^\circ\text{C}$  is metastable and has been described in the orthorhombic system with the space group  $P_{2,2,2_1}$  ( $n^\circ 19$ ) and cell parameters  $a = 5.536(1) \text{ \AA}$ ,  $b = 9.231(1) \text{ \AA}$ ,  $c = 10.170(1) \text{ \AA}$ . <sup>[37,47]</sup> This allotropic variety is isostructural to  $\text{Nd}_2\text{TeO}_6$

and appears to be metastable.<sup>[48]</sup> and can be described with distorted isolated  $[\text{WO}_6]$  and two different types of polyhedra for the neodymium: a square-triangle polyhedron  $[\text{Nd}(1)\text{O}_7]$  and a monocapped trigonal prism  $[\text{Nd}(2)\text{O}_6]$  (**figure 1 b**).

Finally, the third polymorph at high temperature ( $T > 1450^\circ\text{C}$ ), has been first indexed by Yoshimura *et al.* in a tetragonal cell closely related to an ordered fluorite ( $a_q \approx a_F = 5.426\text{\AA}$ ;  $c_q \approx c_F = 8.695\text{\AA}$ ) (**figure 1 c**).<sup>[46, 49]</sup>

Yoshimura *et al.* and Efremov have noticed that all  $\text{Ln}_2\text{WO}_6$  compounds,<sup>[46; 38]</sup> have the same high temperature structural type even if low temperature polymorphs are different. Later, Tyulin *et al.* solved the structure of  $\text{Nd}_{1.2}\text{Lu}_{0.8}\text{WO}_6$  which is isostructural to the  $\text{Ln}_2\text{WO}_6$  high temperature form;<sup>[50]</sup> it crystallizes in the space group  $P4_2/m$  ( $n^\circ 113$ ) with cell parameters  $a = 5.276(1)\text{\AA}$ ;  $c = 8.658(1)\text{\AA}$ . The structure consists of large isolated  $[\text{WO}_6]$  octahedral (**figure 1c**), while the neodymium atoms are in cubic coordination.

In this work, we focus on the growth of  $\text{Nd}_2\text{WO}_6$  thin film by means of pulsed laser deposition (PLD) on (100)-oriented  $\text{SrTiO}_3$  (STO) substrate. Advanced microstructural characterizations carried out by X-ray diffraction (XRD) and Transmission electron microscopy (TEM) reveal the stabilization of a new  $\text{Nd}_2\text{WO}_6$  polymorph, hereafter labelled alpha. Nanoscale ferroelectricity is highlighted in this new oxide thin film by carefully investigating electrical properties using Atomic Force Microscopy tools and, more specifically, the Piezoresponse Force Microscopy (PFM) and Conductive-AFM (c-AFM) modes.

## EXPERIMENTAL METHODS

A  $\text{Nd}_2\text{WO}_6$  ceramic pellet, 1 inch in diameter and 5 mm-thick, was used as target for laser ablation. The ceramic was prepared by solid-state reaction route method, mixing dried oxides  $\text{Nd}_2\text{O}_3$  and  $\text{WO}_3$  (Sigma Adrich, purities of 99.9%) weighted in stoichiometric proportions. Twice, with an intermediate grinding, the mixture was heated at  $1350^\circ\text{C}$  in air for one night. The resulting powder was then ground, pressed in the form of a disc using an uni-axial press, sintered up to  $1450^\circ\text{C}$  for 12h in air and slowly cooled down to room temperature. The XRD pattern confirms the synthesis of a pure powder of the low temperature polymorph of  $\text{Nd}_2\text{WO}_6$  that was afterward used as target.<sup>[31]</sup>

The depositions as thin film form by PLD were carried out with a Compex Pro 102 KrF excimer laser ( $\lambda = 248\text{ nm}$ ) on (100)-oriented STO single-crystal substrates (Crystal GmbH, Germany). The fluence was adjusted to  $2\text{ J/cm}^2$  and the deposition rate was  $2\text{ Hz}$ . The target-substrate distance was adjusted to  $d = 4.5\text{ cm}$ . All substrates were first ultrasonically cleaned in ethanol for 5 minutes, and then dried. The pressure in the pulsed-laser chamber was lowered down to  $10^{-4}\text{ Pa}$ . Then, the substrate temperature was raised through a  $10^\circ\text{C/min}$  step elevation to the growth temperature, *i.e.*  $900^\circ\text{C}$  under a dynamical  $\text{O}_2$  pressure of  $10^{-1}\text{ mbar}$ , while the depostion corresponds to

12000 laser-pulse shots. Finally,  $\text{O}_2$  gas was introduced into the chamber (200 mBar) and the film was slowly cooled down to room temperature.

The bulk-powder X-ray diffractograms were obtained using a Rigaku Ultima IV equipped with a Cu-anode X-ray tube ( $\lambda K_\alpha = 1.5418\text{\AA}$ ). The thin films crystalline nature (indexation, rocking curves and Reciprocal Space Maps (RSMs)) were characterized using a Rigaku SmartLab X-ray diffractometer equipped with a 9 kW rotating anode X-ray generator and a copper anode. For  $\omega$ -2 $\theta$  and rocking curves analysis,  $\phi$ -scan and RSMs, a high resolution configuration was used: the X-Ray beam was made parallel with a cross-beam optics and monochromatized with a double Ge (220) monochromator. In this study all the ( $\omega$ -2 $\theta$ ) scans were performed in the range of  $10$ - $90^\circ$ , with a step size of  $0.02^\circ$  and a  $1^\circ/\text{min}$  speed whereas the  $\Phi$ -scan was acquired in the range of  $-10$ - $360^\circ$ , with a step size of  $0.4^\circ$  and a  $40^\circ/\text{min}$  speed. Pole figure measurements were made in medium resolution configuration coupled, *i.e.* without the monochromator ( $\lambda K_\alpha = 1.5418\text{\AA}$ ) using a  $0.5^\circ$  grazing incidence and an in-plane geometry.

The TEM images were obtained using a Hitachi HF-3300 equipped with a cold field emission gun operated at 300 kV, an image aberration corrector (CEOS B-COR) and a  $4\text{ k}\times 4\text{ k}$  camera (Gatan Oneview). Cross-section electron transparent thin foils were prepared using a dual beam machine (scanning electron microscope and focused gallium ion beam) FEI Helios.

PFM and c-AFM experiments were performed with an AFM microscope (MFP-3D, Asylum Research/Oxford Instruments) at room temperature and under ambient conditions to get access to the local electrical properties. Ti/Ir-coated tip and cantilever with a nominal  $\sim 2.8\text{ N.m}^{-1}$  spring constant (ASYELEC-01, Asylum Research) were used. PFM analysis were carried out by using dual AC resonance tracking (DART) mode to enhance the detected electromechanical signal.<sup>[51]</sup> PFM in spectroscopic mode was conducted by applying a driving voltage of 2V to the local probe. The piezoloops were recorded in remnant mode, *i.e.* voltage pulses are applied to the active layer and the PFM signal is measured at zero field. Such measurements promote electromechanical activity against electrostatic interaction.<sup>[52]</sup> Poling experiments were performed by applying DC voltages of  $\pm 10\text{ V}$  to the probe tip. Further details can be found elsewhere.<sup>[53]</sup> For c-AFM measurements, the probe tip was grounded and the bias voltage was applied to the bottom electrode.

## RESULTS AND DISCUSSION

### X ray diffraction phase

In order to characterize the crystalline quality of the films,  $\omega$ -2 $\theta$  diffractograms were collected (see **Fig.2a**). Several well-defined peaks are observed, corresponding to both substrate (in black) and film (in red). As already reported in the literature and summarized in the introduction part of this paper, depending on the

temperature, three allotropic varieties of  $\text{Nd}_2\text{WO}_6$  can be stabilized as long as powders are concerned (reminder: low temperature form is monoclinic  $C_2^2$  with  $a = 5.55(1)$  Å,  $b = 11.38(1)$  Å,  $c = 15.86(1)$  Å,  $\beta = 107.7^\circ$ , it is orthorhombic  $P_{2,2,2}$ ,  $a = 5.536(1)$  Å,  $b = 9.231(1)$  Å,  $c = 10.170(1)$  Å at intermediate temperature and finally tetragonal  $P\bar{4}_2m$ ,  $a = 5.276(1)$  Å;  $c = 8.658(1)$  Å for the high temperature polymorph). By comparison with ICDD-PDF cards, we identified the growth direction of the film with a parameter around 8.68 Å, i.e. either the  $\bar{c}$  direction of the high temperature  $\text{NdWO}$  tetragonal variety, or the  $\bar{c}$  direction of the high temperature polymorph  $\alpha\text{-LaWO}$ , orthorhombic.<sup>[41]</sup> Indeed, the two high temperature varieties ( $\text{NdWO}$ -tetragonal and  $\text{LaWO}$  orthorhombic) are strongly related, and only the  $a$  parameter differs between them:  $a_{\text{LWO-ortho}} \sim 3 \times a_{\text{NdWO-tetra}}$ ;  $b_{\text{LWO-ortho}} \sim b_{\text{NdWO-tetra}}$ ;  $c_{\text{LWO-ortho}} \sim c_{\text{NdWO-tetra}}$ . However, at this step, since only  $00l$  peaks are visible, it is not possible to discriminate them.

In the case of  $\text{La}_2\text{WO}_6$ ,<sup>[41]</sup> we have already shown that starting from a target containing the low temperature polymorph, PLD technique stabilizes the high temperature polymorph. It is important, in the present unknown case of  $\text{Nd}_2\text{WO}_6$  to conclude on the true symmetry of the structure and know if the film is either tetragonal or orthorhombic. In addition, if the majority of the diffraction peaks can be attributed to only one  $00l$  growth direction, the two peaks at  $2\theta = 32.47^\circ$  and  $68.13^\circ$ , attributed to  $(5\ 1\ 0)$  and  $(10\ 2\ 0)$  orientations respectively, indicate that another domain has also grown on the substrate. It is possibly due to the increasing refractory behavior of Nd compared to La, and the fact that the maximum of temperature that our heater can reach is  $T_{\text{max}} = 900^\circ\text{C}$ . To answer this open complex question, we decide to make a complete XRD study.

Considering  $a_{\text{STO}} = 3.905$  Å for commercial STO substrates (Crystal GmbH), and  $a_{\text{NdWO}} = b_{\text{NdWO}} = 5.426$  Å (by referencing to the Yoshimura results on the tetragonal  $\text{NdWO}$  form),<sup>[46]</sup> the lattice mismatch between the film and the substrate can be calculated as follows:

$$\delta = \frac{a_{\text{STO}} \times \sqrt{2} - a_{\text{NdWO}}}{a_{\text{STO}} \times \sqrt{2} \times 100} \quad \text{Equation [1]}$$

The quite low value of the lattice mismatch,  $\delta = 1.7\%$ , i.e. meaning low tensile strains induced by the substrate in the plane of the film, indicates a possible matching of  $a_{\text{NdWO}}$  on a  $(100)\text{-STO}$  allowing an expected good crystalline quality of the thin film growth.

#### Epitaxy relationship

In order to further investigate the thin film quality, rocking curves on both  $(001)$ -peak of the STO substrate and  $(002)$ -peak of the  $\text{NdWO}$  thin film were recorded (**Fig.2b**). The  $0.17^\circ$  full width at half-maximum (FWHM) value measured for  $\text{NdWO}$ , with respect to the  $0.07^\circ$  one obtained for the substrate, indicates a relatively good crystalline quality with a weak disorientation of the

coherent domains observed along the thin film growth direction.

To get better insight in the characterization of the microstructural properties of our  $\text{NdWO}$  thin films,  $\phi$  scan of the  $(101)$  and  $(011)$  reflections in the tetragonal hypothesis (in green on the **Fig. 3**) indexed as  $(301)$  and  $(011)$  with orthorhombic hypothesis (in black on the **Fig. 3**), have been recorded. Those specific reflections were chosen because of their relatively high intensities and their position quite isolated from substrate ones. Whatever the symmetry, these planes diffract at  $2\theta_{\text{Bragg}} = 19.19^\circ$  and the  $\chi$  angle between  $(001)$  and  $(301)/(011)$  is  $59.25^\circ$  (calculated from Carine software<sup>[54]</sup>). As expected for an epitaxial growth, four peaks are observed on these scans, with a  $90^\circ$  angular-gap between two consecutive ones, in agreement with simulation made by Stereopole software in the case of tetragonal or orthorhombic symmetry.<sup>[55]</sup>

Unfortunately, at this step, it is still not sure if the  $\text{NdWO}$  thin film crystallizes either in the tetragonal cell or in the  $3 \times a$  superstructure orthorhombic. In order to verify this point, a RSM were recorded on the area of the assumed  $(5\ 2\ 1)$  reflection, peak that exists only if the cell is orthorhombic (it would lead to a non-integer  $(2.5\ 2\ 1)$  peak in the tetragonal hypothesis). Since, we observed some non-negligible intensity in this area, it proves that the  $\text{NdWO}$  thin film is orthorhombic (**Fig. 4a**).

In a second time, we located the exact positions (after optimization of the phi and chi angles) of the  $(301)$  ( $2\theta = 19.22^\circ$ ) and  $(011)$  ( $2\theta = 19.20^\circ$ ) reflections in order to extract the film  $a$  and  $b$  cell parameters. The  $c$ -lattice parameter value was indeed previously calculated from the  $2\theta$ -omega diffractogram given in **fig.2a**, i.e.  $c = 8.68$  Å. The  $a$  and  $b$  film parameters were deduced from the  $2\theta$  values, leading to  $16.34(5)$  Å and  $5.46(5)$  Å respectively. By comparison with the ones of  $\alpha\text{-LaWO}$  ( $a = 16.56(1)$  Å,  $b = 5.72(1)$  Å;  $c = 8.87(1)$  Å), an 8% decrease of the cell volume is observed. This is in accordance with the evolution observed for the cell volume of the  $\text{Ln}_2\text{WO}_6$  series with the rare earth radii.

Finally, to investigate the “clamping” state of  $\alpha\text{-NdWO}$  thin film on the substrate, a last RSM was recorded around the  $[001]^*$  node of the STO, close to the  $[002]^*$  node of the film: a perfect vertical alignment between the thin film and the substrate is observed (**Fig. 4b**). It means that the film is perfectly clamped on the substrate, in other words that substrate imposes its in-plane parameters to the in-plane ones of the film.

Epitaxial relationships were deduced from examination of the pole-figure measurements on the  $(315)$ -film  $2\theta$  position, position that allowed to observe on the same figure both  $(315)$  peaks from the film and  $(112)$  reflection from the substrate. The comparison between the observed and calculated density of poles, using the Stereopole software,<sup>[55]</sup> shows that  $\text{NdWO}$  thin film adopts the following epitaxial relationships:  $[100]_{\text{NdWO}} \parallel [110]_{\text{STO}}$ ,  $[010]_{\text{NdWO}} \parallel [\bar{1}\bar{1}0]_{\text{STO}}$  and  $[001]_{\text{NdWO}} \parallel [001]_{\text{STO}}$  (**Fig. S11**) i.e. the same 3-D heteroepitaxy as  $\alpha\text{-LWO}$ .



**Figure 5a** presents a TEM image of the thin film cross-section, while inset picture shows is a high-resolution image of the lattice at the interface, confirming that the film is epitaxially grown. **Figure 5b** shows Fourier transforms calculated in the three regions indicated by squares. The region number 1 corresponds to the STO substrate. The regions number 2 and 3, in the film, correspond to domains with two different orientations. As already pointed out on the 2-theta/omega XRD scan (**Figure 3a**), beside  $00\ell$  peaks,  $510$  and  $10\ 2\ 0$  peaks are observed, allowing easy identification of the spots in the vertical direction. Thus, regions number 2 and 3 correspond to a  $(510)$  and a  $(001)$  orientation, respectively. **Figure 5c** presents a color-coded map that showing the distribution of the two types of domains in the layer, identifiable by triangular or trapezoidal shape on the image for the  $(510)$ -oriented domains. It appears that these  $(510)$ -domains (red color) are randomly distributed in the  $(001)$ -oriented matrix (green color), except at the interface with the substrate, where the  $(510)$  orientation is found to be preferred.

As a partial conclusion of this detailed structural and microstructural study, we showed that, by leveraging the PLD method, it is possible to stabilize a new  $\text{Nd}_2\text{WO}_6$  polymorph, isostructural to  $\alpha\text{-La}_2\text{WO}_6$ , which we will hereafter name  $\alpha\text{-Nd}_2\text{WO}_6$ .

#### Nanoscale piezo-/ferroelectric properties

AFM surface morphology of the synthesized film is presented on **Figure 6a**. The  $8 \times 8\ \mu\text{m}^2$  area shows distinct grains and grains boundaries. The grains present irregular shapes with lateral sizes between 100 and 900 nm and a root mean square roughness about 3.6 nm. Nanoscale piezo-/ferroelectric properties have been investigated using PFM tool. Both phase and amplitude loops, recorded in remnant mode for minimizing the electrostatic contribution, are depicted in the inset of the **Figure 6a**. Clear hysteresis with two opposite ferroelectric states are observed from the phase signal with almost  $180^\circ$  phase difference, while typical butterfly-shape is recorded for amplitude response, suggesting local ferroelectricity under the probing tip. However, in the last years, much attention was paid to curious PFM responses recorded on oxide films, i.e. classical PFM loops obtained on non-ferroelectric material, which can be attributed to several phenomena such as Joule heating, electrostriction, chemical dipole, charge injection, field effect, Vegard strain, deposition, subsurface damaging, surface damaging or vacancy ordering.<sup>[56, 57, 58, 59, 60, 61, 62, 63, 64]</sup> Thus, considering the complex nature of the physicochemical phenomena that can exist in such oxide thin films exposed to high electric fields and to accurately verify the ferroelectric-like behavior measured, further PFM analyses were conducted to really confirm that the present response is indeed due to ferroelectricity and not an artifact. More precisely, two strategies currently proposed in the literature were adopted: they consist of probing the bias- and time-dependent hysteresis measurements, as reported by Strelcov *et al.* and Chen *et al.*, respectively.<sup>[65], [66]</sup> In this way, PFM voltage

spectroscopy experiments under different AC driving were firstly carried out. **Figure 6d** displays the evolution of the phase signal by increasing the driving voltage. As observed, the piezoloops are insensitive to the  $V_{AC}$  probing voltage as long as the magnitude is lower than the coercive voltage ( $\sim 5\text{ V}$ ), while we note both a narrowing of the hysteresis for applied  $V_{AC}$  higher than the coercive voltage and the collapse of the loops. This is due to the flipping of the polarization during the experiments which disturbs the PFM signal at such high driving voltages, which agrees with a ferroelectric switching phenomenon, as already shown.<sup>[56, 65]</sup> A time-dependent hysteresis study was also undertaken and the results are depicted on the **Figure 6e**. No dependence of the amplitude PFM signal with respect to the cycling period is observed, consistent with a ferroelectric polarization switching process. This behavior enables to exclude an ionic movement under the probing tip which could occur for longer periods, and thus focus on the dynamics of intrinsic polarization as main factor for the amplitude signals recorded, as previously published.<sup>[66, 67]</sup> These bias- and time-dependent hysteresis measurements represent an essential step to ascribe the hysteresis loops measured by spectroscopic PFM to a pure ferroelectric polarization.

From spectroscopic PFM measurements, the surface deformation amplitude was plotted as a function of various driving AC voltages in order to further confirm the electromechanical nature of the detected signal. As seen on the **Figure 6f**, a linearity is obtained until about 2 V then a saturation is observed, attesting of the piezo-activity of the layer. In the PFM mode, the local deformation amplitude  $A$  measured by the probing tip is proportional to the amplitude of the AC voltage  $V_{AC}$ , the quality factor  $Q$  and the effective piezoelectric coefficient  $d_{33}^{eff}$ , i.e.  $A = d_{33} \times V_{AC} \times Q$ . For contact resonance, the amplitude signal is enhanced and  $Q$  is usually ranging from 30 to 100,<sup>[68]</sup> but for such inorganic  $\text{NdWO}$  compound the loss is considered as rather low which leads to a high value for  $Q$ , typically of about 70–100. Considering the slope of the positive linear part of the plot in **Figure 6f** is 185 pm/V (the linearly fitted line leads to  $y = 185x$  with  $r^2 = 0.9762$ ), we can estimate the effective piezoelectric coefficient between 1.9 and 2.6 pm/V. Note that it is only an estimation and that it is important to consider that the amplitude response is strongly dependent of the measurement location over the free surface of the film. Besides, the clamping of the film on the substrate can lead to an underestimation of the determined value. In addition, it is also well-known that the electric field beneath the AFM probing tip is inhomogeneous in such PFM experiments, leading to quantitative measurements of signal particularly difficult.<sup>[69]</sup> However, the essential point to keep in mind is that even if it is not possible to give an accurate value for the local  $d_{33}^{eff}$ , the estimated value we measured for deformations (1.9–2.6 pm/V) are promising in view of the development of future lead-free piezoelectric systems based on  $\text{Ln}_2\text{WO}_6$  family.

Switching behavior was then studied by means of poling experiments using PFM lithography. Artificial domains were locally induced by applying a DC voltage of +10 and -10 V to the AFM tip over rectangular area at the free surface of the film, then out-of-plane PFM signals were measured. As seen on **Figure 6b**, strong bright and dark contrasts are obtained for the phase PFM image corresponding to domains with 'upward' (away from the substrate) and 'downward' (toward the substrate) polarization, respectively. Amplitude vibration is revealed by the high contrasts seen on the **Figure 6c**, while domain boundaries are highlighted by the absence of amplitude signal due to the switch of polarization. The AFM morphology (**Figure 6a**) simultaneously recorded with PFM images does not reveal any change on the surface, excluding surface electrochemical processes during writing step.<sup>[70]</sup>

The retention properties of the locally manipulated ferroelectric domains were then investigated. For that, two 'artificial' domains with reverse polarization were first formed by applying  $\pm 10$  V between the AFM tip and the grounded substrate, as revealed by the contrasted out-of-plane PFM phase signal on the **Figure 7b**. The tip-induced polarizations were then probed during one day after poling and the obtained signals are presented on the **Figures 7b-d** (see **Fig. S12** for detailed signal evolution). First, no correlation is observed between the surface morphology (**Figure 7a**) and the corresponding PFM images (**Figure 7b**), excluding surface reaction to mainly explain such contrasts, while clear blue and yellow contrasts are observed even after 24h. Also, we can observe some regions with lower contrast from 8h after poling, particularly for positively polarized areas (blue regions), and this contrast decreases with time until 24h, suggesting relaxation phenomena, although contrasted areas remain. The study of the time-dependent back-switched domains was performed in view of determining the characteristic time  $\tau$  which is a strong indication on the parameter governing the PFM contrasts, *i.e.* either intrinsic polarization or mediated by the field-induced ion migration in the bulk of the film. The **Figure 7e** depicts the fraction percentage of switched domains as a function of time. As already reported, we have fitted the relaxation evolution of manipulated domains by means of the following relation:<sup>[71, 67]</sup>

$$f(t) = f_0 + A \exp\left(-\frac{t}{\tau}\right) \quad \text{Equation (2)}$$

with  $f(t)$  the fraction of reversed domain correlated to time  $t$ ;  $f_0$  the final percentage of written domains and  $A$  the final percentage of back-switched domains. The dashed line in **Figure 7e** represents the fitting curve according to **Equation 2** for values of  $f_0$  and  $A$  of 90.2 and 9.8%, respectively. We can extract a value for  $\tau$  of about 30 min which is in good agreement with values already published for other 'true' ferroelectric oxides.<sup>[71, 67]</sup> Such value for the time required to nucleate a reverse domain

demonstrates the nonvolatile nature and represents an another proof for ferroelectricity.

Considering both topographic AFM and phase PFM images, relaxed regions (highlighted by the white dotted circles in **Figure 7a**) correspond to surface heterogeneities and especially to the grain boundaries. However, the back-switching does not occur to the created domain walls, in contrast to previous reported studied on other ferroelectrics thin films,<sup>[71, 72]</sup> except for a relaxation time of about 24h. As a consequence, the common starting point for manipulated domain relaxation seems to be a surface heterogeneity like grain boundaries which act as nucleation sites. This phenomenon was already observed in  $\text{Pb}(\text{Zr}_{0.2}\text{Ti}_{0.8})\text{O}_3$  thin films.<sup>[73]</sup> Moreover, it is well-known the grains boundaries present very high default density, such as oxygen vacancy which particularly exist in transition-metal oxides. Numbers of works demonstrated the ferroelectric domain retention was directly impacted by the oxygen defects into the active layer.<sup>[74, 75, 76]</sup> Indeed, these vacancies play a major role on the domain wall mobility, this mobility being directly related to the relaxation dynamic. Besides, mainly positively manipulated domains (blue contrasts) show relaxation. This can be explained by the presence of surface heterogeneities mentioned above on these poled regions. However, this behavior is mainly supported by the fact that these domains were just positively polarized, while two consecutively reverse polarizations were applied to the other domains. Indeed, some studies have reported a better retention behavior for poled domains when the polarization was reverse switched.<sup>[72, 77, 78]</sup> Also, the decrease of contrast can be attributed to the depolarization field or owing the domains switched under the tip which might not extend throughout the whole film thickness.<sup>[79]</sup>

As a consequence, these poling studies both confirm the room temperature stability of the ferroelectricity and reveal a typical behavior of ferroelectric domains relaxation.

Then, from both the specific relaxation behavior for manipulated domains and the inability to perform classical P-E hysteresis measurements on these thin films (mainly due to high current leakages), we undertook to locally probe eventual leakage currents into the NdWO layer. The nanoscale conductivity was measured by using c-AFM technique. Current maps were recorded by scanning the same region with the grounded tip and by varying the bias voltage between -10 and +10 V to the bottom electrode. Images measured at -7 V, -8 V, -9 V and -10 V are presented on **Figure 8b-e**. Differences in conduction properties are observed, as evidenced by the conducting paths in blue contrast. For relatively high voltages (ranging from +10 down to -7 V), the detected current is insignificant, as revealed on **Figure 8b**. From -8 V, local leakage begins to be detected at several locations, corresponding to 'hot spots' (blue regions in **Figure 8c**). By increasing bias (absolute value), most of

the existing conducting regions extend and new conducting paths appear as seen on **Figures 8d** and **8e**, indicating the local conductivity is bias-dependent. Black and white dashed circles on the **Figures 8c** and **8e** highlight areas where current clearly extends or where new conducting channels appear, respectively. In addition, obvious correlation between c-AFM contrasts and grain boundaries seen on the associated topographic image (**Figure 8a**) is revealed. Indeed, most of the conductive areas are located between the grains, as particularly observed on **Figure 8e**, while the grain regions do not exhibit significant leakage. A careful interpretation of such current signal located at grain boundaries must be done since a convolution effect with the tip can occur inducing such contrasted areas. Considering the contrasts take only place from a high negative threshold bias, we can reasonably conclude that potential convolution effect between the probe tip and the topography is not the main factor leading to highly conductive zones. Therefore, the local conduction in our NdWO film is found to be mainly dominated by the grain boundaries. Such phenomenon was already observed in ferroelectric oxide thin film as Pb(ZrTi)O<sub>3</sub>, La-doped BiFeO<sub>3</sub> or BiFeO<sub>3</sub>.<sup>[80, 81, 82]</sup> The profile of leakage currents with the corresponding topography signal along the same line (dashed yellow line in **Figures 8a** and **e**) is displayed in **Figure 8f**, where an unambiguous correlation between the local conduction and the grain boundaries is demonstrated. In addition, we notice that current intensity is not directly proportional to the depth of the grain boundaries, which excludes the tip-sample convolution as being responsible of the obtained conductivity map. Strong current leakage in grain boundaries involves higher defect density in these zones, such as positively charged oxygen vacancies. Indeed, grain boundaries can act as reservoirs for the accumulation of oxygen vacancies and, as previously mentioned, such transition-metal oxides commonly present high oxygen vacancy rate.<sup>[82, 83]</sup> Under external bias voltages, a rearrangement of these vacancies occurs which increases their density in the grain boundaries. Consequently, conducting paths appear at these specific locations. Then, by increasing the bias, the charged oxygen vacancies migrate into the NdWO layer in order to reach a new thermodynamic equilibrium, associated to continuous variation of oxygen vacancy distribution.<sup>[84]</sup> Since the rate of oxygen vacancy diffusion along the grain boundaries is almost five orders of magnitude superior to one of the inner parts of the grains,<sup>[81]</sup> the current in the grain boundaries increases more rapidly, leading to the specific local current pattern obtained. These observations are very interesting by considering the retention behavior of the polarization discussed above (see **Fig. 7**). Indeed, in both cases the charged defects located at the grain boundaries, and more precisely the oxygen vacancies, can be responsible for the physical phenomena occurring at the nanoscale. As a remark, the observed conduction at grain boundaries is not uniform, i.e. each grain boundary does not reveal conductivity. It can be explained by the different degrees of angle mismatch of each grain boundaries owing the two

different crystallographic orientations seen on the XRD pattern (**Figure 2**). Indeed, in this case the strain and interfacial energies should differ for different grain boundaries inducing higher defect density, highlighted by electrical hot spots.<sup>[80, 85]</sup>

Besides, since our NdWO film presents local ferroelectric properties, the application of the high external bias voltage during c-AFM analyses modifies the electric polarization and gives rise to the growth of ferroelectric domains beneath the tip through the extension of the existing domain walls. By increasing the electric field, the domain walls extend towards the grains center. Since no significant current is detected into the grains, as shown on **Figure 8e**, no conductivity is observed at the typical location of ferroelectric domain walls at the contrary of works focused on BiFeO<sub>3</sub> or PbZrTiO<sub>3</sub> thin films for example.<sup>[86, 87, 88, 89, 90]</sup> This is reinforced by the current map measured after the manipulation of ferroelectric domains (see **Figure 6b**), where no change in the current pattern was obtained. Consequently, the local conduction is further confirmed to be mainly grain boundaries dependent.

## CONCLUSION

A new polymorph of  $\alpha$ -Nd<sub>2</sub>WO<sub>6</sub> has successfully been isolated and fully characterized from a structural and ferroelectric point of view. This compound was stabilized in thin film form by taking advantage of the substrate-induced strain during the PLD growth. A particular attention has been paid on the structural characterization of the film by carrying out various experiments by high-resolution XRD including  $\omega$ -2 $\theta$ , rocking curves,  $\phi$  scan, pole figure and RSMs on well-targeted nodes. By carefully choosing a discriminant reciprocal space node, we demonstrated that this new  $\alpha$ -Nd<sub>2</sub>WO<sub>6</sub> polymorph is orthorhombic, isostructural to the high-temperature of bulk  $\alpha$ -La<sub>2</sub>WO<sub>6</sub>.<sup>[41]</sup> By performing bias- and time-dependent PFM hysteresis experiments, and by achieving poling measurements, the local piezo-/ferroelectricity behavior was carefully demonstrated. The room temperature stability of the ferroelectric polarization was also shown. The nanoscale mapping of the conductivity has revealed to be bias-dependent and dominated by the grain boundaries. Higher defect density such as the accumulation of charged oxygen vacancies in combination with their good mobility in the grain boundaries under external electric field mainly explained the specific local conduction, as well as the polarization relaxation phenomena observed.

Consequently, our results extracted from PFM imaging and spectroscopic mode evidence robust intrinsic ferroelectricity into the NdWO layer at the nanoscale level. This finding extends the piezo-/ferroelectric behavior to a second compound belonging to the A<sub>2</sub>WO<sub>6</sub> family (A = lanthanide), the first one being LaWO.<sup>[41, 42]</sup>

As a consequence, our findings show the strain-engineering as a useful strategy for inducing novel functionalities within oxide thin films, and they

particularly allow for extending the class of lead-free ferroelectric materials.

FIGURES.

**Figure 1.** Temperature-dependence of  $\text{Nd}_2\text{WO}_6$  bulk crystal-structures. Structure projection of (a) low temperature monoclinic  $\text{Nd}_2\text{WO}_6$  with  $[\text{WO}_6]$  blocs; (b) orthorhombic high temperature  $\text{Nd}_2\text{WO}_6$  allotropic variety with isolated  $[\text{WO}_6]$  polyhedral and (c) high temperature tetragonal  $\text{Nd}_2\text{WO}_6$  form which is isostructural to  $\text{Nd}_{1.2}\text{Lu}_{0.8}\text{WO}_6$  from Yoshimura results. [46]

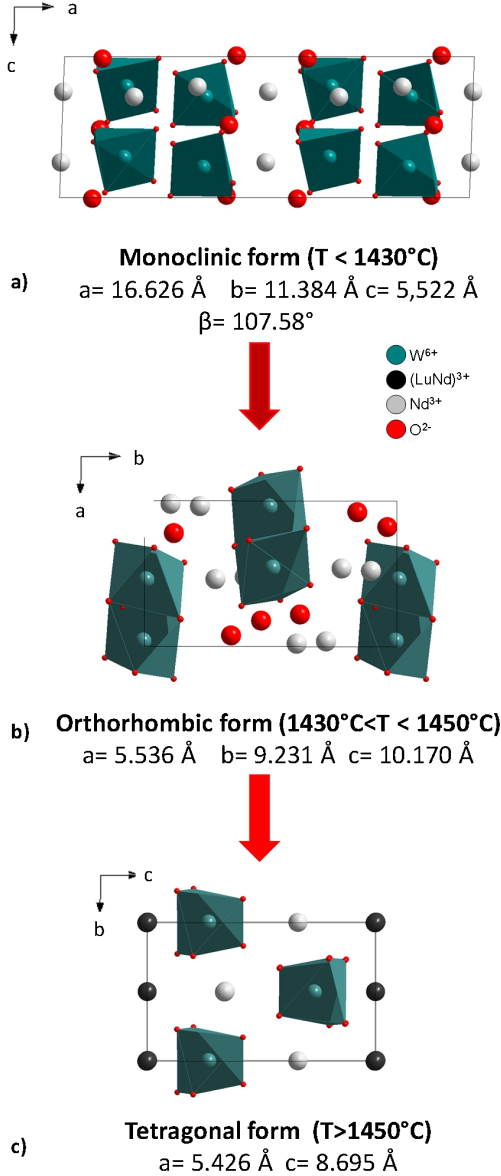


**Figure 2.** X-ray diffractograms on  $\text{Nd}_2\text{WO}_6$  thin films. (a)  $\omega$ - $2\theta$  X-ray diffractogram of epitaxial  $\text{Nd}_2\text{WO}_6$  thin film grown at  $T = 900^\circ\text{C}$  and  $\text{PO}_2 = 10^{-4}\text{mbar}$ . (b) Normalized rocking curves on (002)  $\text{NdWO}$  thin film and on (001) STO substrate (FWHM are indicated in insert).

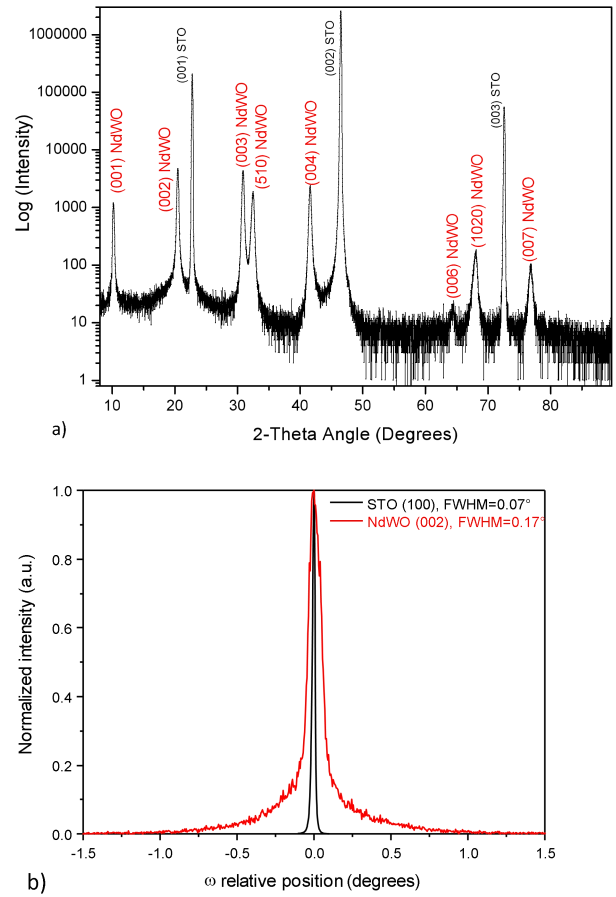


**Figure 3.** Phi-scan for  $\text{Nd}_2\text{WO}_6$  on (101)/(011) peak in case of tetragonal cell (in green) or (301)/(011) peak on orthorhombic hypothesis (in black). Four peaks are observed; peak repetition rate is  $180^\circ$ .

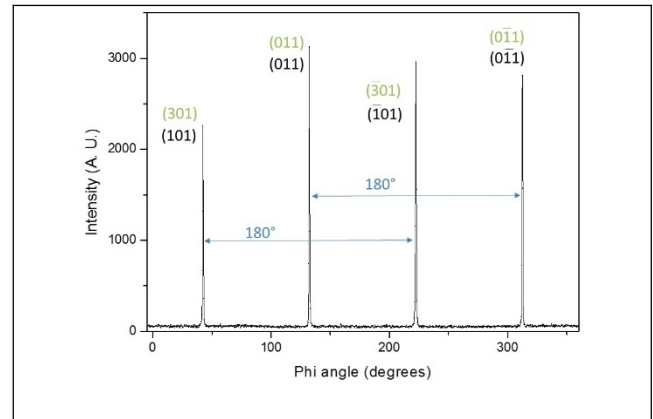


**Figure 4.** Reciprocal space maps along nodes of  $\text{NdWO}$  thin film and STO substrate. (a) Reciprocal space map along  $[521]^*$   $\text{Nd}_2\text{WO}_6$  highlighting finally the orthorhombic structure of the thin film as  $\alpha\text{-La}_2\text{WO}_6$ . (b) Reciprocal space map, along  $[001]^*$  STO and  $[002]^*$   $\alpha\text{-NdWO}$ .

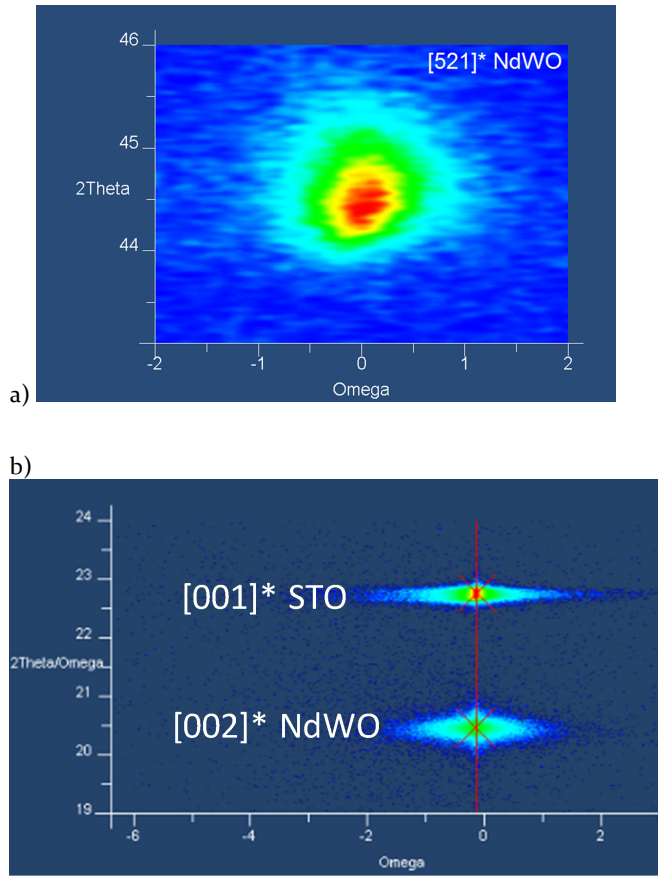


**Figure 5.** Transmission electron microscopy images of the  $\text{Nd}_2\text{WO}_6$  film. (a) TEM image of the film cross-section. Inset shows a high resolution image of the epitaxial interface. (b) Fourier transforms obtained in the three regions indicated by squares. (c) Color-coded map that shows the spatial distribution of the two types of domains in the image (a). (510)-oriented domains are red and (001)-oriented domains are green. The map was created by applying filters to the corresponding spots in Fourier space.

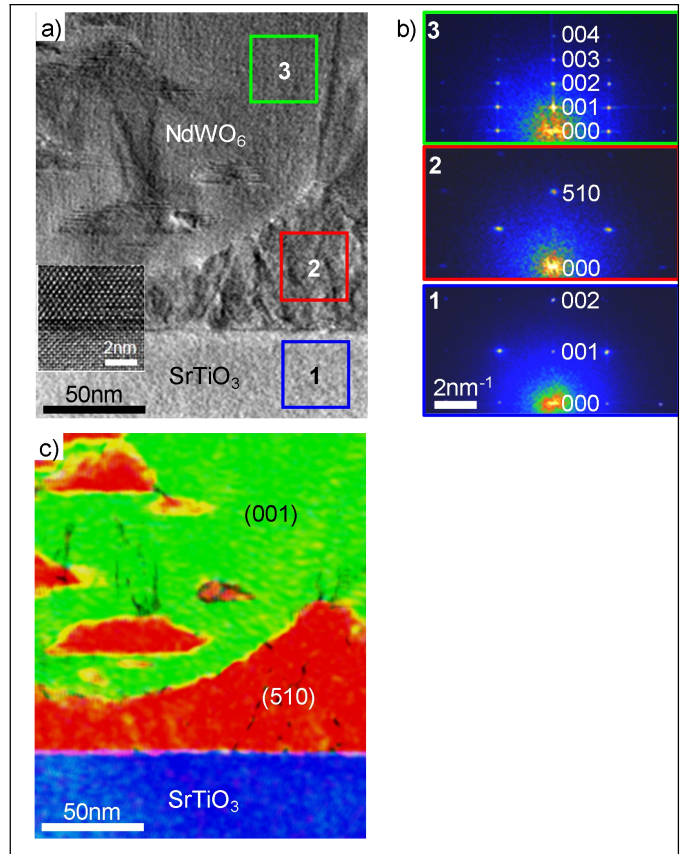


**Figure 6.** Nanoscale piezo-/ferroelectric behavior and bias- and time-dependent hysteresis measurements properties performed on  $\text{Nd}_2\text{WO}_6$  thin film. (a) AFM morphology simultaneously measured with out-of-plane (b) phase and (c) amplitude PFM images after poling experiments. The inset of the (a) shows the local remnant phase and amplitude piezoresponse loops recorded on the free surface of the  $\text{NdWO}$  thin film. (d) Phase PFM loops under different AC driving voltage, (e) and amplitude PFM loops for different period time. (f) AC voltage dependence of the local surface displacement of the  $\text{NdWO}$  layer. The regression plot between 0 and 2 V corresponding to the linear part (highlighted by the blue rectangular) leads to an effective piezoelectric coefficient between 1.9 and 2.6 pm/V.



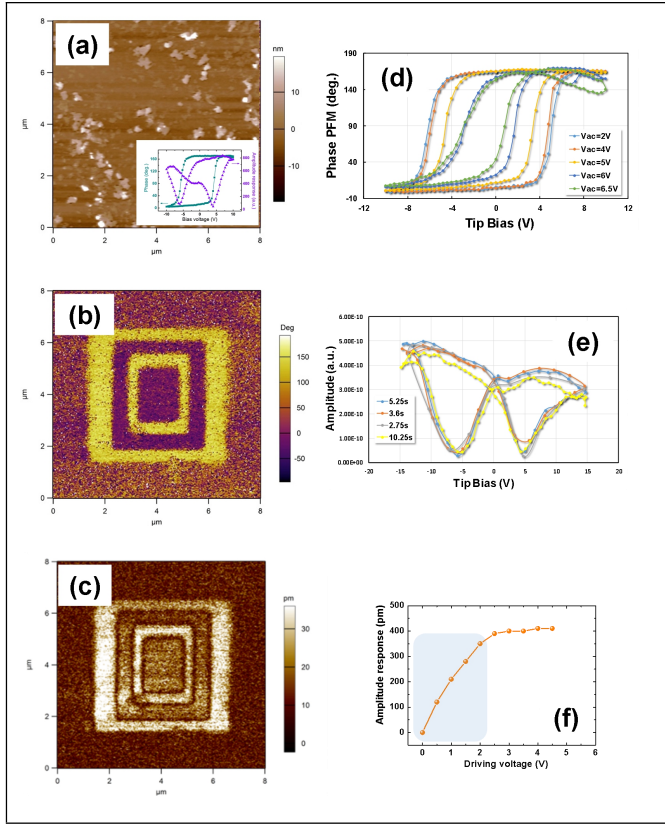


**Figure 7.** Time-dependence of the locally manipulated domains. (a) AFM morphology and out-of-plane phase PFM signals recorded (b) just after, (c) 8h after, and (d) one day after the poling experiment at  $\pm 10$  V. Scale bars of phase signal are similar for all of PFM images. White dotted circles on AFM image denote the surface heterogeneities acting as nucleation sites for reverse domains. (e) Percentage of reversed domains as a function of time. Dashed line corresponds to the fitting curve according to Equation 2, leading to characteristic time value of about 30 min.

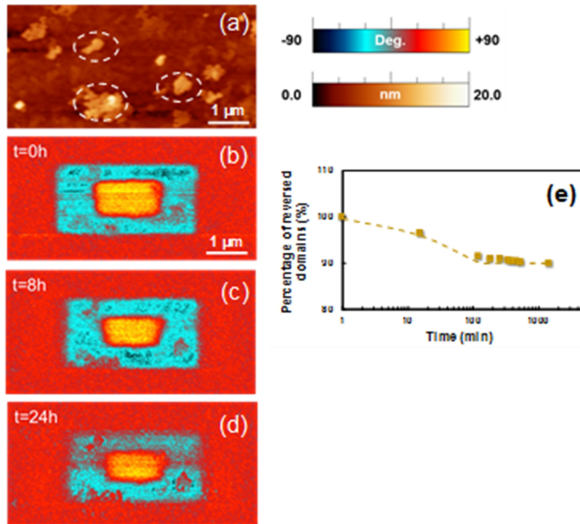
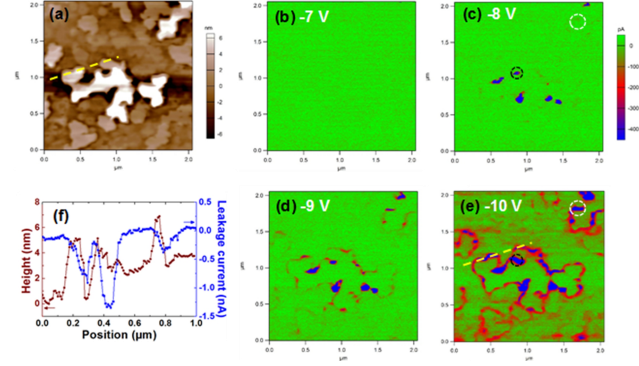


**Figure 8.** Local conduction in  $\text{Nd}_2\text{WO}_6$  thin film. (a) AFM topography, and current maps of the corresponding  $\text{NdWO}$  surface recorded with bias voltages of (b)  $-7$  V, (c)  $-8$  V, (d)  $-9$  V and (e)  $-10$  V. Higher conductivity is detected when larger bias voltage is applied. (f) Current signal and associated topography profile along the yellow dotted lines in (a) and (e), indicating the correlation between the local leakages and the grain boundaries. Scale bars for the current intensity are similar for all c-AFM images.



## ASSOCIATED CONTENT

**Figure SI1.**  $\alpha$ - $\text{Nd}_2\text{WO}_6$  (315) Pole figure, illustrating the orientation relationship between  $\text{STO}$ -(100) substrate and  $\alpha$ - $\text{Nd}_2\text{WO}_6$  thin film.

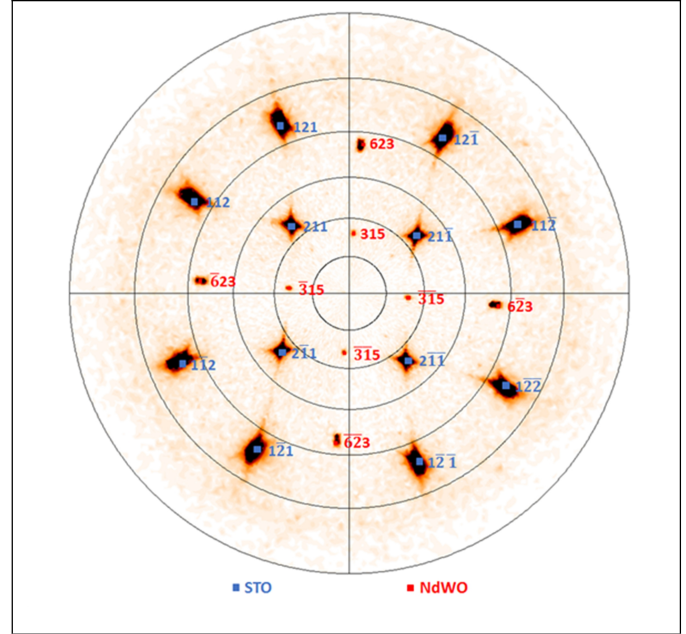
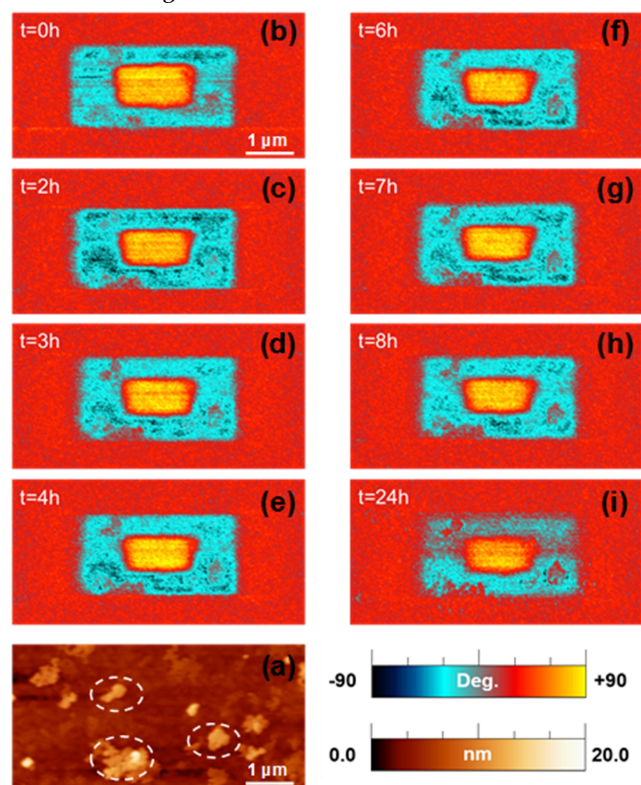


**Figure SI2.** Time-dependence of the locally manipulated domains. (a) AFM morphology and (b-i) out-of-plane phase PFM signals recorded during one day after the poling

experiment at  $\pm 10$  V. Scale bars of phase signal are similar for all of PFM images.



## AUTHOR INFORMATION

### Corresponding Author

\* MH Chambrier : mhelene.chambrier@univ-artois.fr

### Present Addresses

†If an author's address is different than the one given in the affiliation line, this information may be included here.

### Author Contributions

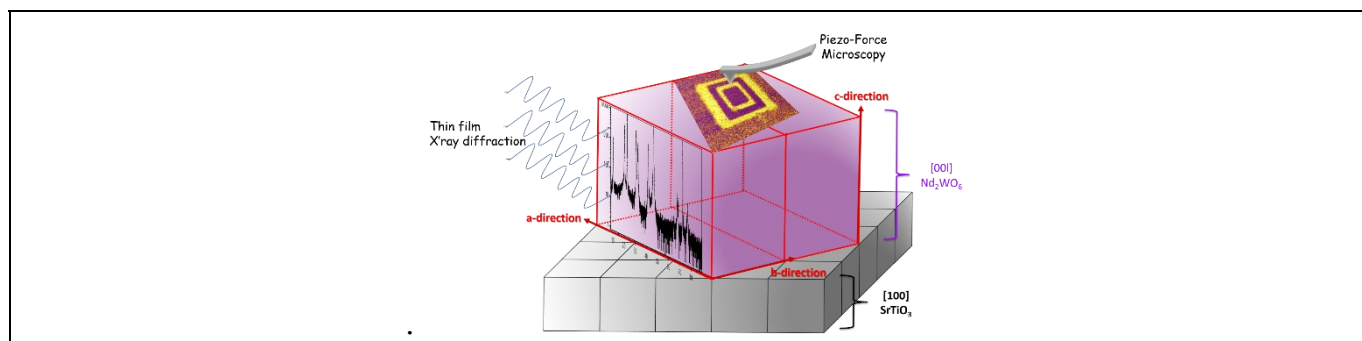
The manuscript was written through contributions of all authors. / All authors have given approval to the final version of the manuscript. / ‡These authors contributed equally.

### Funding Sources

Any funds used to support the research of the manuscript should be placed here (per journal style).

## ACKNOWLEDGMENT

Chevreur Institute (FR 2638), Ministère de l'Enseignement Supérieur, de la Recherche et de l'Innovation, Hauts-de-France Region, Fonds Européen de Développement Régional (FEDER) and Major Domain of Interest (DIM) "Eco-Energy Efficiency" of Artois University are acknowledged for supporting and funding partially this work. FEDER, CNRS, Hauts-de-France Region and Ministère de l'Education Nationale de l'Enseignement Supérieur, de la Recherche et de l'Innovation are acknowledged for fundings of X-ray diffractometers. Région Hauts-de-France and FEDER are gratefully acknowledged for funding the MFP-3D microscope under Program "Chemistry and Materials for a Sustainable Growth".



## REFERENCES

- <sup>1</sup> Nagarajan, V.; Roytburg, A.; Stanishevsky, A.; Prasertchoung, S.; Zhao, T.; Chen, L.; Melngailis, J.; Auciello, O.; Ramesh, R., Dynamics of Ferroelastic Domains in Ferroelectric Thin Films. *Nat. Mater.* **2002**, *2*, 43-47.
- <sup>2</sup> Vrejoiu, I.; Le Rhun, G.; Pintilie, L.; Hesse, D.; Alexe, M.; Gösele, U., Intrinsic Ferroelectric Properties of Strained Tetragonal  $\text{PbZr}_{0.2}\text{Ti}_{0.8}\text{O}_3$  Obtained on Layer-by-Layer Grown, Defect-Free Single Crystalline Films. *Adv. Mater.* **2006**, *18*, 1657-1661.
- <sup>3</sup> Leclerc, G.; Domengès, B.; Poullain, G.; Bouregba, R., Elaboration of (111)-oriented La-doped PZT Thin Films on Platinized Silicon Substrates. *Appl. Surf. Sci.* **2006**, *253*, 1143-1149.
- <sup>4</sup> Detalle, M.; Ferri, A.; Da Costa, A.; Desfeux, R.; Soyer, C.; Rémiens, D., Nanoscale Study by Piezoresponse Force Microscopy of Relaxor  $0.7\text{Pb}(\text{Mg}_{1/3}\text{Nb}_{2/3})\text{O}_3-0.3\text{PbTiO}_3$  and  $0.9\text{Pb}(\text{Mg}_{1/3}\text{Nb}_{2/3})\text{O}_3-0.1\text{PbTiO}_3$  Thin Films Grown on Platinum and  $\text{LaNiO}_3$  Electrodes. *Thin Solid Films* **2010**, *518*, 4670-4674.
- <sup>5</sup> Saito, Y.; Takao, H.; Tani, T.; Nonoyama, T.; Takatori, K.; Homma, T.; Nagaya, T.; Nakamura, M. Lead-free piezoceramics, *Nature* **2004**, *432*, 84-87.
- <sup>6</sup> Shvartsman, V. V.; Pertsev, N. A.; Herrero, J.M.; Zaldo, C.; Kholkin, A. L. Nonlinear local piezoelectric deformation in ferroelectric thin films studied by scanning force microscopy, *Journal of Applied Physics* **2005**, *97*, 104105.
- <sup>7</sup> Zhang, S.; Xia, R.; Shrout, T. R. Lead-free piezoelectric ceramics vs. PZT? *Journal of Electroceramics* **2007**, *19*, 251-257.
- <sup>8</sup> Uchino, K. Ferroelectric devices; Taylor and Francis Group, 2010.
- <sup>9</sup> EU-Directive 2002/96/EC: Waste Electrical and Electronic Equipment (WEEE); *Off. J. Eur. Union* **2003**, *46*, [L37], 24-38.
- <sup>10</sup> EU-Directive 2002/95/EC: Restriction of the Use of Certain Hazardous Substances in Electrical and Electronic Equipment (RoHS); *Off. J. Eur. Union* **2003**, *46*, [L37], 19-23.
- <sup>11</sup> Rödel, J.; Jo, W.; Seifert, K. T. P.; Anton, E.-M.; Granzow, T. Perspective on the development of Lead-Free Piezoceramics. *J. Am. Ceram. Soc.* **2009**, *92* [6], 1153-1177.
- <sup>12</sup> Wu, J.; Xiao, D.; Zhu, J. Potassium – Sodium Niobate Lead-Free Piezoelectric Materials: Past, Present, and Future of Phase Boundaries. *Chemical Review* **2015**, *115*, 2559-2595.
- <sup>13</sup> Acosta, M.; Novak, N.; Rojas, V.; Patel, S.; Vaish, R.; Koruza, J.; Rossetti, G. A.; Rödel, J.  $\text{BaTiO}_3$ -based piezoelectrics: Fundamentals, current status, and perspectives. *Applied Physics Reviews* **2017**, *4*, 041305.
- <sup>14</sup> Becher, C.; Maurel, L.; Aschauer, U.; Lilienblum, M.; Magén, C.; Meier, D.; Langenberg, E.; Trassin, M.; Blasco, J.; Krug, I. P.; Algarabel, P. A.; Spaldin, N. A.; Pardo, J. A.; Fiebig, M. Strain-Induced Coupling of Electrical Polarization and Structural Defects in  $\text{SrMnO}_3$  Films. *Nature Nanotechnology* **2015**, *10*, 661-665.
- <sup>15</sup> Haeni, J. H.; Irvin, P.; Chang, W.; Uecker, R.; Reiche, P.; Li, Y. L.; Choudhury, S.; Tian, W.; Hawley, M. E.; Craigo, B.; Tagantsev, A. K.; Pan, X. Q.; Streiffer, S. K.; Chen, L. Q.; Kirchhofer, S. W.; Levy, J.; Schlom, D. G. Room-Temperature Ferroelectricity in Strained  $\text{SrTiO}_3$ . *Nature* **2004**, *430*, 758-761.
- <sup>16</sup> Lu, H.; Lee, D.; Klyukin, K.; Tao, L.; Wang, B.; Lee, H.; Lee, J.; Paudel, T. R.; Chen, L.-Q.; Tsymbal, E. Y.; Alexandrov, V.; Eom, C.-B.; Gruverman, A. Tunneling Hot Spots in Ferroelectrics  $\text{SrTiO}_3$ . *Nano Lett.* **2018**, *18*, 491-497.
- <sup>17</sup> Lee, J. H.; Fang, L.; Vlahos, E.; Ke, X.; Jung, Y.W.; Kourkoutis, L. F.; Kim, J.-W.; Ryan, P.J.; Heeg, T.; Roeckerath, M.; Goian, V.; Bernhagen, M.; Uecker, R.; Hammel, P. C.; Rabe, K. M.; Kamba, S.; Schubert, J.; Freeland, J.W.; Muller, D. A.; Fennie, C. J.; Schiffer, P.; Gopalan, V.; Johnston-Halperin, E.; Schlom, D. G. A Strong Ferroelectric Ferromagnet Created by means of Spin-Lattice Coupling. *Nature* **2010**, *466*, 954-958.
- <sup>18</sup> Ranjith, R.; Mangalam, R.V.K.; Boullay, Ph.; David, A.; Lepetit, M.B.; Lüders, U.; Prellier, W.; Da Costa, A.; Ferri, A.; Desfeux, R.; Vincze, G.; Radi, Z.; Aruta, C. Constrained ferroelectric domain orientation in  $\text{BiFeO}_3/\text{SrTiO}_3$  heterostructures. *Applied Physics Letters* **2010**, *96*, 022902.
- <sup>19</sup> Liu, W.; Ren, X. Large piezoelectric effect in Pb-free ceramics. *Physical Review Letters* **2009**, *103*, 257602.
- <sup>20</sup> Shvartsman, V. V.; Lupascu, D. C. Lead-Free Relaxor Ferroelectrics. *J. Am. Ceram. Soc.* **2012**, *95* [1], 1-26.
- <sup>21</sup> Shrout, T. R.; Zhang, S. J. Lead-free piezoelectric ceramics: Alternatives for PZT?, *J Electroceram* **2007**, *19*, 111-124.
- <sup>22</sup> Lv, Y.; Yao, W.; Zong, R.; Zhu, Y. Fabrication of wide range-visible photocatalyst  $\text{Bi}_2\text{WO}_6$ -x nanoplates via surface oxygen vacancies. *Scientific reports* **2016**, *6*, 19347.
- <sup>23</sup> Wolfe, R.W.; Newnham, N.E.; Kay, M.I. Crystal Structure of  $\text{Bi}_2\text{WO}_6$ . *Solid State Comm.* **1969**, *7*, 1797.



- <sup>24</sup> Lacorre, P.; Goutenoire, F.; Bohnke, O.; Retoux, R.; Laligant, Y. Designing Fast Oxide-Ion Conductors Based on  $\text{La}_2\text{Mo}_2\text{O}_9$ . *Nature* **2000**, *404*, 856-858.
- <sup>25</sup> Amsif, M.; Magrasó, A.; Marrero-López, D.; Ruiz-Morales, C.; Canales-Vásquez, J.; Núñez, P. Mo-Substituted Lanthanum Tungstate  $\text{La}_{(28-y)}\text{W}_{(4+y)}\text{O}_{54+8}$ : A Competitive Mixed Electron-Proton Conductor for Gas Separation Membrane Applications. *Chem. Mater.* **2012**, *24*, 3868-3877.
- <sup>26</sup> Amano, F.; Nogami, K.; Abe, R.; Ohtani, B. Preparation and Characterization of Bismuth Tungstate Polycrystalline Flake-Ball Particles for Photocatalytic Reactions. *J. Phys. Chem. C* **2008**, *112* (25), 9320-9326.
- <sup>27</sup> Janulevicius, M.; Marmokas, P.; Misevicius, M.; Grigorjevaite, J.; Mikoliunaite, L.; Sakirzanovas, S.; Katelnikovas, A. Luminescence and luminescence quenching of highly efficient  $\text{Y}_2\text{Mo}_4\text{O}_{15}:\text{Eu}^{3+}$  phosphors and ceramics. *Scientific Reports* **2016**, *6*, 26098.
- <sup>28</sup> Sleight, A. W.; Thundathil, M. A.; Evans, J. S. O. Negative Thermal Expansion Materials. The State of Oregon on Behalf of Oregon State University, Corvallis, USA 1995.
- <sup>29</sup> Borchardt, H.J.; Bierstedt, P. E. Ferroelectric Rare Earth Molybdates. *J. Chem. Phys.* **1967**, *38*, 2057-2060.
- <sup>30</sup> Flippen, R. B.; Hogan, E. M. Mechanical transducers using coupled ferroelectric-ferroelastic crystals, *US Patent Appl* N°428,717, **1973**.
- <sup>31</sup> Brixner, L. H.; Sleight, A. W.; Foris, C. M. Refined Cell parameters of the  $\text{Ln}_2\text{WO}_6$ -Type Rare Earth Tungstates. *J. of solid States Chem.* **1973**, *7*, 418.
- <sup>[32]</sup> Efremov, V. A.; Tyulin, A. V. Polymorphism of Oxytungstates  $\text{Tr}_2\text{WO}_6$ . Mechanism of Structural Changes of  $\text{Er}_2\text{WO}_6$ . *Kristallografiya* **1987**, *32*, 363-370.
- <sup>[33]</sup> Efremov, V. A.; Tyulin, A. V. Polymorphism of Oxytungstates  $\text{Tr}_2\text{WO}_6$ . Analysis of Structural Type II ( $\text{Gd}_2\text{WO}_6$  and  $\text{Gd}_2\text{MoO}_6$ ). Mechanism of Structural Change in  $\text{Gd}_2\text{WO}_6$  in the Phase Transition II  $\leftrightarrow$  V. *Kristallografiya* **1987**, *32*, 371-377.
- <sup>[34]</sup> Polyanskaya, T. M.; Borisov, S. V.; Belov, N. V. A New Form of the Scheelite Structural Type: Crystal Structure of  $\text{Nd}_2\text{WO}_6$ . *Dokl. Akad. Nauk SSSR* **1970**, *193*, 83-86.
- <sup>[35]</sup> Tyulin, A. V.; Efremov, V. A.; Trunov, V. K. Polymorphism of Oxytungstates  $\text{Tr}_2\text{WO}_6$ . Mechanisms of Structural Changes in  $\text{Y}_2\text{WO}_6$ . *Crystallogr. Rep.* **1989**, *34*, 531-536.
- <sup>[36]</sup> Efremov, V. A.; Tyulin, A. V.; Trunov, V. K.; Kudin, O. V.; Yanovskii, V. K.; Voronkova, V. I. The Crystal Structure of Monoclinic  $\text{Y}_2\text{WO}_6$  and  $\text{Yb}_2\text{WO}_6$ . *Kristallografiya* **1984**, *29*, 904-909.
- <sup>37</sup> Borchardt, H. J. Rare-Earth Tungstates and 1:1 Oxytungstates. *Journal of Chemical Physics* **1963**, *39*, 3, 504.
- <sup>38</sup> Efremov, V. A. Characteristic features of the crystal chemistry of lanthanide molybdates and tungstates. *Russian Chemical Reviews* **1990**, *59* (7), 627-642.
- <sup>[39]</sup> Chambrier, M.-H.; Kodjikian, S.; Ibberson, R. M.; Goutenoire, F. Ab-initio Structure Determination of  $\beta\text{-La}_2\text{WO}_6$ . *J. Solid State Chem.* **2009**, *182*, 209-214.
- <sup>[40]</sup> Allix, M.; Chambrier, M. H.; Veron, E.; Porcher, F.; Suchomel, M.; Goutenoire, F. Synthesis and Structure Determination of the High Temperature Form of  $\text{La}_2\text{WO}_6$ . *Cryst. Growth Des.* **2011**, *11*(6), 2528-2539.
- <sup>41</sup> Carlier, T.; Chambrier, M.-H.; Ferri, A.; Estrade, S.; Blach, J.F.; Martin, G.; Meziane, B.; Peiro, F.; Roussel, P.; Ponchel, F.; Rémiens, D.; Cornet, A.; Desfeux, R. Lead-Free  $\alpha\text{-La}_2\text{WO}_6$  Ferroelectric Thin Films. *ACS Appl. Mater. Interfaces* **2015**, *7*, 24409-24418.
- <sup>42</sup> Carlier, T.; Chambrier, M.-H.; Ferri, A.; Bayart, A.; Roussel, P.; Saitzek, S.; Desfeux, R. Microstructure and local electrical investigation of lead-free  $\alpha\text{-La}_2\text{WO}_6$  ferroelectric thin films by piezoresponse force microscopy. *Thin Solid Films* **2016**, *639*, 841-851.
- <sup>43</sup> Apostolov, Z. D.; Sarin, P.; Hughes, R. W.; Kriven, W. M. Thermal Expansion of  $\text{Ln}_6\text{WO}_{12}$  and  $\text{Ln}_2\text{WO}_6$  -An *In Situ* Synchrotron X-ray Diffraction Study. *J. Am. Ceram. Soc.* **2014**, *97*, 2496-2505.
- <sup>[44]</sup> Zhijun, Z.; Hui, Z.; Jun, D. C.; Lin, Y. J.; Xiaojun, W.; Bang, X. D.; Hong, C. H.; Tai, Z. J. Structure refinement  $\text{Lu}_2\text{WO}_6$  and luminescent properties of  $\text{Eu}^{3+}$ ,  $\text{Pr}^{3+}$  doped  $\text{Lu}_2\text{WO}_6$ . *J. of Alloys and Compounds* **2008**, *466*, 258-263.
- <sup>45</sup> Beaury, O.; Faucher, M.; Teste de Sagey, G.; Caro, P. Investigation of a new structural type for  $\text{Y}_2\text{WO}_6$ . *Mat. Res. Bull.* **1978**, *13*, 953-957.
- <sup>46</sup> Yoshimura, M.; Sibieude, F.; Rouanet, A.; Foëx, M. Polymorphism of  $\text{R}_2\text{O}_3\text{-WO}_3$  (R = Rare Earth) compounds at high temperatures. *Rev. int. Htes Temp. et Réfract.* **1975**, *12*, 215.
- <sup>47</sup> Efremov, V.A.; Tyulin, A. V.; V. K. Trunov. The structure of a new modification of  $\text{Nd}_2\text{SO}_6$ , *Kristallografiya* **1984**, *29*, 673-676.
- <sup>[48]</sup> Meier, S. F.; Schleid, Th. Crystal structure of dineodymium(III) hexaoxotellurate(VI),  $\text{Nd}_2\text{TeO}_6$ . *Z. Kristallogr. NCS* **2004**, *219*, 359-360.
- <sup>[49]</sup> Yoshimura, M.; Rouanet, A.; Sibieude, F.; Foëx, M. Phases de haute température des tungstates de lanthanides du type  $\text{Ln}_2\text{O}_3\text{-WO}_3$  (Ln = La, Ce, Nd, Sm, Dy et Y). *C. R. Acad. Sci. C. Fr.* **1974**, *279*, 863-865.
- <sup>[50]</sup> Tyulin, A. V.; Efremov, V. A.; Trubov, V. K. Polymorphism of  $\text{Ln}_2\text{WO}_6$  oxytungstates. Structure of  $\text{Nd}_{1.2}\text{Lu}_{0.8}\text{WO}_6$ . *Kristallografiya* **1989**, *34*, [1], 81-86.
- <sup>51</sup> Rodriguez, B.J.; Callahan, C.; Kalinin, S. V., Proksch, R. Dual-frequency resonance tracking atomic force microscopy. *Nanotechnology* **2007**, *18*, 1-6.
- <sup>[52]</sup> Qiao, H.; Seol, D.; Sun, C.; Kim, Y. Electrostatic contribution to hysteresis loop in piezoresponse force microscopy. *Appl. Phys. Lett.* **2019**, *114*, 152901.
- <sup>[53]</sup> Desfeux, R.; Ferri, A.; Legrand, C.; Maës, L.; Da Costa, A.; Poullain, G.; Bouregba, R.; Soyer, C.; Remiens, D. Nanoscale investigations of switching properties and piezoelectric activity in ferroelectric thin films using piezoresponse force microscopy. *Int. J. Nanotechnol.* **2008**, *5*, 827-837.
- <sup>[54]</sup> CaRIne Crystallography, version 3.1.
- <sup>[55]</sup> Stéréopole
- <sup>[56]</sup> Balke, N.; Maksymovych, P.; Jesse, S.; Herklotz, A.; Tselev, A.; Eom, C.-B.; Kravchenko, I. I.; Yu, P.; Kalinin, S. V. Differentiating Ferroelectric and Nonferroelectric Electronmechanical Effects with Scanning Probe Microscopy. *ACS Nano* **2015**, *9*, 6484-6492.
- <sup>[57]</sup> Vasudevan, R.K.; Balke, N.; Maksymovych, P.; Jesse, S.; Kalinin, S.V. Ferroelectric or non-Ferroelectric: Why So Many Materials Exhibit "Ferroelectricity" On The Nanoscale. *Appl. Phys. Rev.* **2017**, *4*, 021302.

- [58] Seol, D.; Kim, B.; Kim, Y. Non-Piezoelectric Effects in Piezoresponse Force Microscopy. *Current Applied Physics* **2017**, *17*, 661-674.
- [59] Martin, S.; Baboux, N.; Albertini, D.; Gautier, B. Interpretation of Multiscale Characterization Techniques to Assess Ferroelectricity: The Case of GaFeO<sub>3</sub>. *Ultramicroscopy* **2017**, *172*, 47-51.
- [60] Bark, C.W.; Sharma, P.; Wang, Y.; Baek, S.H.; Lee, S.; Ryu, S.; Folkman, C.M.; Paudel, T.R.; Kumar, A.; Kalinin, S.V.; Sokolov, A.; Tsybmal, E.Y.; Rzchowski, M.S.; Gruverman, A.; Eom, C.B. Switchable Induced Polarization in LaAlO<sub>3</sub>/SrTiO<sub>3</sub> Heterostructures. *Nano Lett.* **2012**, *12*, 1765-1771.
- [61] Borowiak, A. S.; Baboux, N.; Albertini, D.; Vilquin, B.; Saint Girons, G.; Pelloquin, S.; Gautier, B. Electromechanical Response of Amorphous LaAlO<sub>3</sub> Thin Film probed by Scanning Probe Microscopies. *Applied Physics Letters* **2014**, *105*, 012906.
- [62] Li, C.; Cao, Y.; Bai, Y.; Li, A.; Zhang, S.; Wu, D. Electromechanical Response from LaAlO<sub>3</sub>/SrTiO<sub>3</sub> Heterostructures. *ACS Appl. Mater. Interfaces* **2015**, *7*, 10146-10151.
- [63] Seol, D.; Park, S.; Varenky, O. V.; Lee, S.; Lee, H. N.; Morozovska, A. N.; Kim, Y. Determination of Ferroelectric Contributions to Electromechanical Response by Frequency Dependent Piezoresponse Force Microscopy. *Sci. Rep.*, **2016**, *6*, 30579.
- [64] Carlier, T.; Ferri, A.; Saitzek, S.; Huvé, M.; Bayart, A.; Da Costa, A.; Desfeux, R.; Tebano, A. Microstructure and local electrical behavior in [(Nd<sub>2</sub>Ti<sub>2</sub>O<sub>7</sub>)<sub>4</sub>/(SrTiO<sub>3</sub>)<sub>n</sub>]<sub>10</sub> (n = 4-8) superlattices. *RSC Advances* **2018**, *8*, 11262.
- [65] Strelcov, E.; Kim, Y.; Yang, J. C.; Chu, Y. H.; Yu, P.; Lu, X.; Jesse, S.; Kalinin, S. V. Role of Measurement Voltage on Hysteresis Loop Shape in Piezoresponse Force Microscopy. *Appl. Phys. Lett.* **2012**, *101*, 192902.
- [66] Chen, Q. N.; Ou, Y.; Ma, F.; Li, J. Mechanisms of Electromechanical coupling in Strain Based Scanning Probe Microscopy. *Applied Physics Letters* **2014**, *104*, 242907.
- [67] Guan, Z.; Jiang, Z.-Z.; Tian, B.-B.; Zhu, Y.-P.; Xiang, P.-H.; Zhong, N.; Duan, C.-G.; Chu, J.-H. Identifying Intrinsic Ferroelectricity of Thin Film with Piezoresponse Force Microscopy. *AIP Advances* **2017**, *7*, 095116.
- [68] McLachlan, M.A.; McComb, D.W.; Ryan, M.P.; Morozovska, A.N.; Eliseev, E.A.; Payzant, E.A.; Jesse, S.; Seal, K.; Baddorf, A.P.; Kalinin, S.V. Probing Local and Global Ferroelectric Phase Stability and Polarization Switching in Ordered Macroporous PZT. *Adv. Funct. Mater.* **2011**, *21*, 941-947.
- [69] Gruverman, A.; Alexe, M.; Meier, D. Piezoresponse force microscopy and nanoferroic phenomena, *Nature Communications* **2019**, *10*, 1661.
- [70] Ievlev, A.V.; Maksymovych, P.; Trassin, M.; Seidel, J.; Ramesh, R.; Kalinin, S.V.; Ovchinnikova, O.S. Chemical State Evolution in Ferroelectric Films During Tip-Induced Polarization and Electroresistive Switching. *ACS Applied Materials & Interfaces* **2016**, *8*, 29588-29593.
- [71] Ganpule, C.S.; Nagarajan, V.; Ogale, S.B.; Roytburd, A.L.; Williams, E.D.; Ramesh, R. Domain Nucleation and Relaxation Kinetics in Ferroelectric Thin Films. *Applied Physics Letters* **2000**, *77*, 3275-3277.
- [72] Ganpule, C.S.; Roytburd, A.L.; Nagarajan, V.; Hill, B.K.; Ogale, S.B.; Williams, E.D.; Ramesh, R.; Scott, J.F. Polarization Relaxation Kinetics and 180° domain Wall dynamics in Ferroelectric Thin Films. *Physical review B* **2001**, *65*, 014101.
- [73] Gruverman, A.; Tokumoto, H.; Prakash, A.S.; Aggarwal, S.; Yang, B.; Wuttig, M.; Ramesh, R.; Auciello, O.; Venkatesan, T. Nanoscale Imaging of Domain Dynamics and Retention in Ferroelectric Thin Film. *Applied Physics Letters* **1997**, *71*, 3492.
- [74] Kitanaka, Y.; Noguchi, Y.; Miyayama, M. Oxygen-Vacancy-Induced 90°-Domain Clamping in Ferroelectric Bi<sub>4</sub>Ti<sub>3</sub>O<sub>12</sub> single crystals. *Physical review B* **2010**, *81*, 094114.
- [75] Yamamoto, K.; Kitanaka, Y.; Suzuki, M.; Miyayama, M.; Noguchi, Y.; Moriyoshi, C.; Kuroiwa, Y. High-Oxygen-Pressure Crystal Growth of Ferroelectric Bi<sub>4</sub>Ti<sub>3</sub>O<sub>12</sub> single crystals. *Applied Physics Letters* **2007**, *91*, 162909.
- [76] Lee, J.H.; Shin, R.H.; Jo, W. Polarization Switching and Relaxation Dynamics of Bismuth layered Ferroelectric Thin Films: Role of Oxygen Defect sites and Crystallinity. *Physical review B* **2011**, *84*, 094112.
- [77] Kim, T.Y.; Lee, J.H.; Oh, Y.J.; Choi, M.R.; Jo, W. Charge Retention Behavior of Preferentially Oriented and Textured Bi<sub>3.25</sub>La<sub>0.75</sub>Ti<sub>3</sub>O<sub>12</sub> Thin Films by Electrostatic Force Microscopy. *Applied Physics Letters* **2007**, *90*, 082901.
- [78] Lee, J. H.; Choi, M. R.; Oh, Y. J.; Jo, W. Local Retention Behaviors of Epitaxial and Polycrystalline PbMg<sub>1/3</sub>Nb<sub>2/3</sub>O<sub>3</sub>-PbTiO<sub>3</sub> Thin Films by Scanning Force Microscopy. *Applied Physics Letters* **2007**, *91*, 072906.
- [79] Mazet, L.; Bachelet, R.; Louahadj, L.; Albertini, D.; Gautier, B.; Cours, R.; Schamm-Chardon, S.; Saint-Girons, G.; Dubourdieu, C. Structural Study and Ferroelectricity of Epitaxial BaTiO<sub>3</sub> Films on Silicon Grown by Molecular Beam Epitaxy. *J. Appl. Phys.* **2014**, *116*, 214102.
- [80] Masuduzzaman, M.; Xie, S.; Chung, J.; Varghese, D.; Rodriguez, J.; Krishnan, S.; Alam, M.A. The Origine of Broad Distribution of Breakdown Times in Polycrystalline Thin Film Dielectrics. *Applied Physic Letters* **2012**, *101*, 153511.
- [81] Zhou, M.-X.; Chen, B.; Sun, H.-B.; Wan, J.-G.; Li, Z.-W.; Liu, J.-M.; Song, F.-Q.; Wang, G.-H. Local Electrical Conduction in Polycrystalline La-Doped BiFeO<sub>3</sub> thin Films. *Nanotechnology* **2013**, *24*, 225702.
- [82] Shen, X.; Yin, K.; Puzyrev, Y.S.; Liu, Y.; Sun, L.; Li, R.-W.; Pantelides, S.T. 2D Nanovaristors at Grain Boundaries Account for Memristive Switching in Polycrystalline BiFeO<sub>3</sub>. *Advanced Electronic Materials* **2015**, *1*, 1500019.
- [83] Yan, X.; Li, Y.; Zhao, J.; Li, Y.; Bai, G.; Zhu, S. Roles of Grain Boundary and Oxygen Vacancies in Ba<sub>0.6</sub>Sr<sub>0.4</sub>TiO<sub>3</sub> Films for Resistive Switching Device Application. *Applied Physics Letters* **2016**, *108*, 033108.
- [84] Choi, T.; Horibe, Y.; Yi, H.T.; Choi, Y. J.; Wu, W.; Cheong, S.-W. Insulating Interlocked Ferroelectric and Structural Antiphase Domain Walls in Multiferroic YMnO<sub>3</sub>. *Nature Materials* **2010**, *9*, 253-258.
- [85] Read, W.T.; Shockley, W. Dislocation Models of Crystal Grain Boundaries. *Phys. Rev.* **1950**, *78*, 275.
- [86] Seidel, J.; Martin, L.W.; Hei, Q.; Zhan, Q.; Chu, Y.-H.; Rother, A.; Hawkridge, M.E.; Maksymovych, P.; Yu, P.; Gajek, M.; Balke, N.; Kalinin, S.V.; Gemming, S.; Wang, F.; Catalan, G.; Scott, J. F.; Spaldin, N.A.; Orenstein, J.; Ramesh, R. Conduction at Domain Walls in Oxide Multiferroics. *Nature Materials* **2009**, *8*, 229-234.
- [87] Farokhipoor, S.; Noheda, B. Conduction Through 71° Domain Walls in BiFeO<sub>3</sub> Thin Films. *Physical Review Letters* **2011**, *107*, 127601.

- 
- [<sup>88</sup>] Farokhipoor, S.; Noheda, B. Local Conductivity and The Role of Vacancies Around Twin Walls of (001)-BiFeO<sub>3</sub> Thin Films. *Journal of Applied Physics* **2012**, 112, 052003.
- [<sup>89</sup>] Guyonnet, J.; Gaponenko, I.; Gariglio, S.; Paruch, P. Conduction at Domain Walls in Insulating Pb(Zr<sub>0.2</sub>Ti<sub>0.8</sub>)O<sub>3</sub> Thin Films. *Adv. Mater.* **2011**, 23, 5377–5382.
- [<sup>90</sup>] Rojac, T.; Bencan, A.; Drazic, G.; Sakamoto, N.; Ursic, H.; Jancar, B.; Tavcar, G.; Makarovic, M.; Walker, J.; Malic, B.; Damjanovic, D. Domain-Wall Conduction in Ferroelectric BiFeO<sub>3</sub> Controlled by Accumulation of Charged Defects. *Nature Materials* **2017**, 16, 322–328.